https://doi.org/10.5194/egusphere-2026-2626
Preprint. Discussion started: 26 May 2026

MJO Diagnostic Tools v1.1: Reassessment and implementation of standard MJO diagnostic tools in Python

Nijiko Inoue[1], Tamaki Suematsu[2*], Hiroaki Miura[1], Daehyun Kim[3, 4]

[1]Graduate School of Science, The University of Tokyo, Tokyo 113-0033, Japan
[2]RIKEN Center for Computational Science, Kobe, 650-0047, Japan
[3]School of Earth and Environmental Sciences, Seoul National University, Seoul, 08826, South Korea
[4]Department of Atmospheric and Climate Science, University of Washington, Seattle, 98195, USA

Correspondence to: Tamaki Suematsu (tamaki.suematsu@riken.jp)

Abstract

The Madden–Julian Oscillation (MJO) remains difficult to simulate realistically in atmospheric and coupled models, with model performance being strongly dependent on physical parameterizations and model configurations. A standardized and reproducible diagnostic framework of the MJO is therefore essential for systematic evaluation and model development. A widely used set of MJO diagnostics was developed by the US CLIVAR MJO Working Group in 2009 (MJO-WG09), but its original implementation depends on software and workflows that are no longer readily accessible in modern computing environments.

In this study, we reimplement the MJO-WG09 diagnostics using Python-based analysis libraries. The diagnostics are reconstructed following the published methodology and, where necessary, by examining the original source code to resolve ambiguities. As a result of methodological reassessment, the new implementation differs from the original in aspects such as temporal filtering, statistical testing, and spectral analysis; these differences are documented and discussed. In addition, we introduce a new diagnostic to evaluate the Walker circulation associated with the MJO. The open-source package provides a reproducible foundation for consistent evaluation of MJO simulations across models.

1 Introduction

The MJO is recognized as a system of organized convection coupled to large-scale zonal and meridional circulations, which typically initiates over the western to central Indian Ocean and propagates slowly eastward at approximately 5 m s^{-1} (Madden and Julian, 1971, 1972). The organized convection associated with the MJO generally dissipates after passing over the maritime continent and reaching the dateline. Simulations of the MJO have been reported to be challenging using atmospheric general circulation models (AGCMs) or coupled general

https://doi.org/10.5194/egusphere-2026-2626
Preprint. Discussion started: 26 May 2026

circulation models (CGCMs) since the 1990s (Lin et al., 2006; Slingo, 1996). Representations of the MJO in current GCMs and CGCMs are still considered inadequate (Ahn et al., 2020a; Hung et al., 2013; Jiang et al., 2020, 2021; Kim and Maloney, 2017), and results from a CGCM study suggest that the MJO may be spuriously enhanced by air–sea interactions within the model (Chen et al., 2020). The development of global cloud/storm resolving models (GCRMs/GSRMs) was expected to improve MJO representation (Miura et al., 2007). However, subsequent findings suggest that better representation is not achieved simply by using explicit formulations of cloud microphysics but is instead highly sensitive to the tuning of cloud microphysics parameters (Miura, 2019; Takasuka et al., 2024). Meanwhile, the rapid progress in machine learning–based weather forecasting—such as GraphCast, GenCast, and NeuralGCM (Kochkov et al., 2024; Lam et al., 2023; Price et al., 2024)—has given rise to new demands for evaluating the fidelity of MJO representation within these systems.

In this context, the need for a unified framework to evaluate the reproducibility of the MJO across AGCMs, CGCMs, GCRM/GSRMs, and AI-based models can be considered both longstanding and newly emerging. Within the model development community, there was a need for unified evaluations of AGCMs and CGCMs in the 2000s and the US CLIVAR MJO Working Group developed and released the MJO Simulation Diagnostics (Waliser et al., 2009, hereafter MJO-WG09). The MJO Simulation Diagnostics package was first applied to a set of AGCM and CGCM simulations by Kim et al., (2009) and has been widely used within the MJO community. However, the original codes and data provided on the website (https://atmos.uw.edu/~daehyun/mjo_diagnostics/) that hosted the MJO Simulation Diagnostics is no longer accessible.

In response to this situation, we re-implemented a platform for a systematic evaluation of the simulated MJO across models. As a first step, we decided to revive the MJO simulation diagnostic tools released by MJO-WG09. The MJO simulation diagnostic package, previously distributed through the official website, was implemented using Fortran and Grid Analysis Display System (GrADS) which were standard tools for data analysis and visualization at the time. Currently, however, cross-platform usability—particularly of GrADS—has become increasingly limited. Therefore, we chose to reconstruct the diagnostics using Python, which is widely supported and easily used across modern computing environments.

We re-implemented the diagnostics using Python libraries that fit standard workflows. Where the methodology described in MJO-WG09 was ambiguous or lacked sufficient detail, we referred the original source code previously distributed to clarify the intended procedures. As a result of both the adaptation to Python libraries and the re-examination of the original methods, our implementation diverges in several areas—most notably in the application of temporal filtering, statistical testing, and spectral analysis techniques. In this paper, we focus primarily on these differences. We also introduce a new diagnostic to evaluate the Walker circulation, which serves as the background

https://doi.org/10.5194/egusphere-2026-2626
Preprint. Discussion started: 26 May 2026

zonal circulation associated with the MJO and has recently been recognized to significantly influence the MJO behaviour (Suematsu et al., 2022; Suematsu and Miura, 2022; Takasuka et al., 2024). For results that remain broadly consistent with MJO-WG09—aside from minor discrepancies likely due to differences in the datasets—we provide a concise description and include the corresponding figures in Appendix A (Figures A1–A9).

Section 2 describes the Python environment used in this study, including versioning and libraries. Section 3 outlines the sample datasets used for analysis. Section 4 explains the analytical methods. Section 5 is a summary of the reimplemented MJO diagnostic tools.

2 Python environment

The new implementation of MJO Diagnostic Tools were developed in Python version 3.12.4, with additional dependencies on NumPy, xarray, netCDF4 or h5netcdf, Cartopy, Matplotlib, SciPy, math, and SymPy. The input data format is netCDF. The latitude–longitude grid information is not explicitly specified; instead, it is obtained using the xarray library in Python.

3 Data

In this study, observational and reanalysis datasets, rather than model simulations, were used to examine the performance of the newly implemented MJO diagnostic tools. Whenever possible, the same datasets as those employed by MJO-WG09 were used. When the exact datasets were unavailable, comparable datasets for the same variables were substituted.

The MJO diagnostic tool expects eight variables: sea surface temperature (SST), surface precipitation (PRCP), 10m zonal wind (U_{10m}), 10 m meridional wind (V_{10m}), zonal wind (U), meridional wind (V), pressure velocity (ω), and outgoing longwave radiation (OLR). While MJO-WG09 employed surface horizontal winds (i.e., horizontal winds at the lowest model level), we use 10 m horizontal winds to allow for a more direct comparison among models. SST, PRCP, U_{10m}, V_{10m} and OLR are two-dimensional fields, while U, V, and ω are three-dimensional variables defined on 17 pressure levels: 1000, 925, 850, 700, 600, 500, 400, 300, 250, 200, 150, 100, 70, 50, 30, 20, and 10 hPa. Hereafter three-dimensional variables will be denoted with the number of the pressure level following the abbreviation of each variable. For example, U at 850 hPa is denoted as U850. The toolset includes a program to extract specific levels necessary for the analysis (e.g. 1000, 850, and 200 hPa) from the full 17-level datasets.

Data from four sources were used in this study. 1. NOAA Optimum Interpolated SST (Huang et al., 2021) with 0.25° latitude spacing (89.875°S-89.875°N) and 0.25° longitude spacing (0.125°E-0.125°W) spanning 1 September

https://doi.org/10.5194/egusphere-2026-2626
Preprint. Discussion started: 26 May 2026

1981 to 31 December 2005 at daily resolution. The horizontal resolution was reduced to 2.5° latitude spacing (88.625°S–88.875°N) and 2.5° longitude spacing (1.375°E–1.125°W) by extracting the SST value of the nearest point in the original data. 2. CMAP Precipitation (Xie and Arkin, 1997), with 2.5° latitude spacing (88.75°S–88.75°N) and 2.5° longitude spacing (1.25°E–1.25°W), spanning 1 January 1979 to 27 December 2016 at 5-day resolution. The precipitation data were interpolated to daily resolution for this study. 3. NCEP/DOE Reanalysis 2 (Kanamitsu et al., 2002) U, V, and ω, with 2.5° latitude spacing (90°S–90°N) and 2.5° longitude spacing (0°E–2.5°W), and U_{10m}, V_{10m} on Gaussian grid with 94 latitudinal points (88.542°S-88.542°N) and 194 longitudinal points (0°E-1.875°W), spanning 1 January 1979 to 31 December 2016 at daily resolution. 4. NOAA Interpolated Outgoing Longwave Radiation (OLR; Liebmann and Smith, 1996), with 2.5° latitude spacing (90°S–90°N) and 2.5° longitude spacing (0°E–2.5°W), spanning 1 June 1974 to 31 December 2022 at daily resolution.

As noted by Suematsu and Miura (2018), the OLR dataset contains periods with spurious values; however, no special treatment for these data was applied in our Python implementation. Although the datasets share a nominal spatial resolution, the exact grid-point locations and area elements are not always identical. Because the aim of this study is to demonstrate the functionality of the developed diagnostic tools rather than to conduct a rigorous scientific analysis, we did not construct a unified grid or interpolate the data to a common grid.

We also note that in MJO-WG09, various datasets were used, but in some cases the data sources were unspecified and preprocessing procedures were unclear. These issues are clarified in the descriptions of each analysis method.

4. Analysis Methods

As in MJO-WG09, the analyses are divided into Level 1 (Section 4.1) and Level 2 (Section 4.2). Level 1 analysis consists of: mean states of SST, PRCP, and U850 (Section 4.1.1); variances of PRCP and U850 (Section 4.1.2); lag–longitude correlation analysis (Section 4.1.3); and lag–latitude correlation analysis for PRCP and U850 (Section 4.1.4). Level 2 analysis consists of: wavenumber–frequency spectral analyses of PRCP and U850 (Section 4.2.1); cross-spectral analyses of OLR and U850 (Section 4.2.2); multivariate combined Empirical Orthogonal Function (EOF) analysis of OLR, U850, and U200 (Section 4.2.3); and life-cycle composites of U_{10m}, SST, and PRCP (Section 4.2.3). In addition to the analyses conducted in MJO-WG09, we include an analysis of the Walker Circulation in Level 2 (Section 4.2.5).

In this paper, we clarify details that were unclear in the analyses of variances of PRCP and U850, wavenumber-frequency spectral analysis, and EOF analysis in the original MJO-WG09 study. Where different methods were adopted, we explain the rationale behind those choices. For the rest of the MJO-WG09 analyses we found no

https://doi.org/10.5194/egusphere-2026-2626
Preprint. Discussion started: 26 May 2026

essential differences other than those arising from the data used; therefore, only key points are noted here, and the results are presented in Appendix A.

Following MJO-WG09 the analyses were conducted separately for the boreal winter (November–April) and boreal summer (May–October). This separation is considered reasonable for extracting features attributable to geographic factors: during boreal winter, tropical intraseasonal organized cloud systems predominantly propagate eastward (Madden and Julian 1971), whereas during boreal summer, the Eurasian continental heating drives a dominant summer monsoon circulation, within which cloud systems often exhibit northward propagation (Wang and Rui, 1990; Yasunari, 1979).

4.1 Level 1 Diagnostics

4.1.1 Horizontal Maps of Mean States

This analysis examines the mean fields representing the background state of MJO variability. We examine the mean fields of SST (the thermal lower boundary for atmospheric circulation), PRCP (the column-integrated net conversion from latent to sensible heat), and U850 (the large-scale zonal circulation in the tropical troposphere). Unlike MJO-WG09, which used monthly mean SST data, this study employs daily means. The analysis period begins in 1981 instead of 1979 due to changes in data availability. Other procedures follow the original study. Results (Appendix A Figs. A1 and A2) are nearly identical to MJO-WG09.

4.1.2 Horizontal Maps of Intraseasonal Variances

This analysis quantifies the magnitude of variability on intraseasonal time scales. We examine intraseasonal PRCP, an indicator of pronounced upward motion, and intraseasonal U850, which reflects the horizontal wind patterns associated with active convection. In this study, the intraseasonal component is defined by applying a 20–100-day band-pass filter to the PRCP and U850 time series. We adopt the Butterworth filter, available as a Python module, rather than the 201-point Lanczos filter used in the original study. This change has only a minor impact on the results.

The results are shown in Figs. 1 and 2. The black contours indicate the variance of the intraseasonal component, and the shading represents the ratio of intraseasonal variance to the total variance. MJO-WG09 states that their ratio was calculated with the denominator taken as the variance of the 10–180-day band-passed PRCP and the 2–180-day band-passed U850. However, following this method produced ratio values clearly larger than those presented in Figs. 3 and 4 of MJO-WG09. Therefore, in the present study, the denominator was taken as the variance of the unfiltered, data. This yielded values and spatial patterns similar to those in MJO-WG09. Since the choice of

https://doi.org/10.5194/egusphere-2026-2626
Preprint. Discussion started: 26 May 2026

155 denominator only changes the ratio values while maintaining the intended interpretive meaning, the simpler approach is considered sufficient.

For PRCP, some differences remain between our results and those of MJO-WG09. In this study, we used the enhanced version of CMAP PRCP, in which missing values are filled, rather than the standard version employed in MJO-WG09. In addition, we interpolate the PRCP data to daily resolution prior to filtering while MJO-WG09
160 analyses the pentad data directly. These factors are considered the main sources of the discrepancies between the figures.

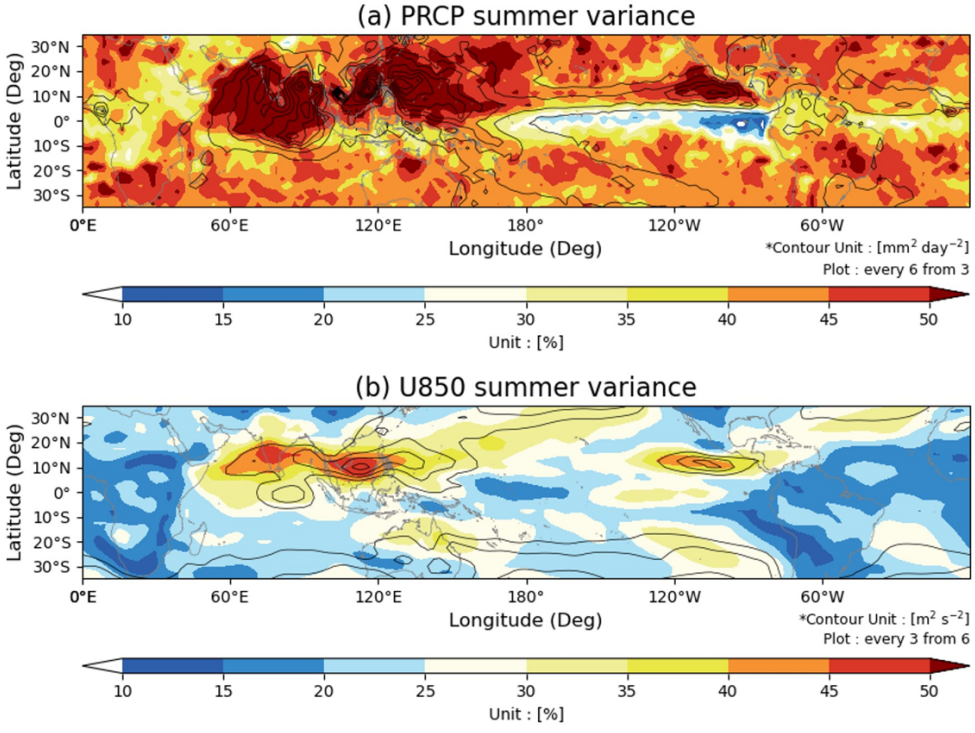

Figure 1 Intraseasonal (20-100day) variances (contours) and its ratio (%) to the variances of the unfiltered data (shades) of (a) PRCP and (b) U850 for May-October season.

165

https://doi.org/10.5194/egusphere-2026-2626
Preprint. Discussion started: 26 May 2026

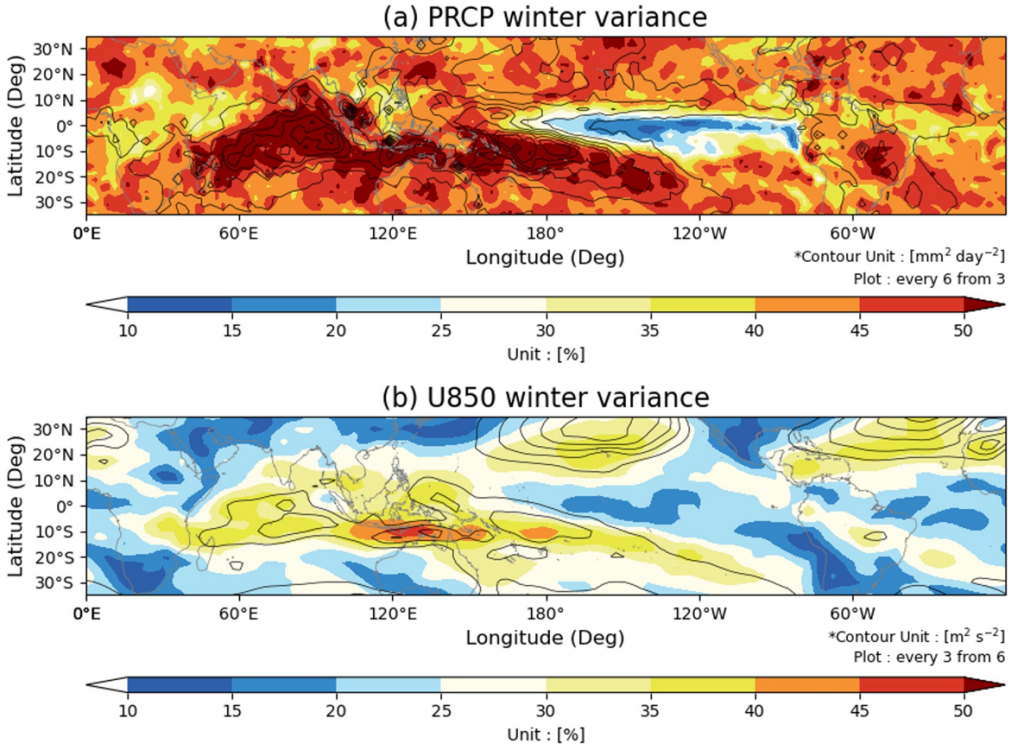

Figure 2 Same as Fig.1 but for November-April season.

4.1.3 Lag–Longitude Correlations

In this analysis, lag–longitude correlations are calculated to determine the spatial scale, propagation speed, and duration of cloud clusters in the east–west direction during boreal winter. To examine the coupling between cloud clusters and the zonal circulation, we analyse PRCP (proxy for active convective activity) and U850. Although MJO-WG09 does not specify the datasets used, we follow the same approach as in previous analyses, using CMAP PRCP and NCEP/DOE U850.

To extract the intraseasonal variability component, a 20–100-day band-pass Butterworth filter is applied. For boreal winter, we compute lag correlations for the time series of one-dimensional latitude–averaged data (averaged over 10°N–10°S), using as a reference the time series of area averaged precipitation over the Indian Ocean reference region (5°N–10°S, 75°E–100°E).

https://doi.org/10.5194/egusphere-2026-2626
Preprint. Discussion started: 26 May 2026

The results are shown in Appendix A Fig. A3. Except for minor differences, they are almost identical to those in MJO-WG09. The differences are likely due to the use of a Butterworth filter instead of a Lanczos filter for extracting intraseasonal variability, and to differences in the interpolation method used to convert PRCP pentad data to daily data.

4.1.4 Lag–Latitude Correlations

While Section 4.1.3 analysed the boreal winter, here we focus on the boreal summer. To depict the spatial scale, propagation speed, and duration of the north–south movement of cloud clusters during boreal summer, we calculate lag–latitude correlations. The datasets used are the same as in Section 4.1.3. The same temporal filter as the lag-longitude analysis is applied, and lag correlations are computed for the time series of one-dimensional latitude–averaged data (averaged over 80°E–100°E), using as a reference the time series of spatially averaged precipitation over the Indian Ocean reference region (5°N–10°S, 75°E–100°E). The results are shown in Appendix A Fig. A4. As in Section 4.1.3, the results closely match those of MJO-WG09.

4.2 Level 2 Diagnostics

4.2.1 Wavenumber–Frequency Spectra

To quantify the space–time characteristics of tropical cloud activity and atmospheric circulation, space–time spectral analysis (Hayashi, 1971) has been widely applied (Takayabu, 1994; Wheeler and Kiladis, 1999). In this analysis, we compute space–time spectra of PRCP, and U850 to illustrate the dominant scales of the MJO.

As MJO-WG09 did not clearly describe other preprocessing steps, we determined them through trial and error. For both boreal winter and boreal summer, PRCP and U850 were averaged over 10°N–10°S at each longitude to produce two-dimensional time–longitude datasets. Each season was defined as a 180-day period (starting from 1 November for boreal winter and 1 May for boreal summer, respectively), yielding 26 boreal winter series (1979–2004) and 27 boreal summer series (1979–2005). The time mean of each 180-day segment is removed and a cosine-tapered rectangular window was applied to zero the first and last 45 days. Spectral analysis of these series produced results comparable to Figs. 7 and 8 of MJO-WG09 (shown here as Figs. 3 and 4). We note that averaging over latitude prior to spectral analysis differs from the method of Wheeler and Kiladis (1999), and we did not compute ratios to background red noise as in their study.

Although the PRCP spectra extend more toward higher wavenumbers than U850, they remain in the range of wavenumbers $k \approx 1$–4, this analysis detects regions of concentrated precipitation on spatial scales much larger than those of individual cumulonimbus clouds. In contrast, U850 exhibits a spectral peak shifted toward lower

https://doi.org/10.5194/egusphere-2026-2626
Preprint. Discussion started: 26 May 2026

wavenumbers. This may be explained as follows: latent heating from organized convection is accompanied by divergent horizontal winds, but these small divergent flows are short-lived. The spectral analysis therefore does not capture them directly; instead, it reflects the flow field achieved by the dissipation of latent heating due to sufficient superpositions of gravity waves.

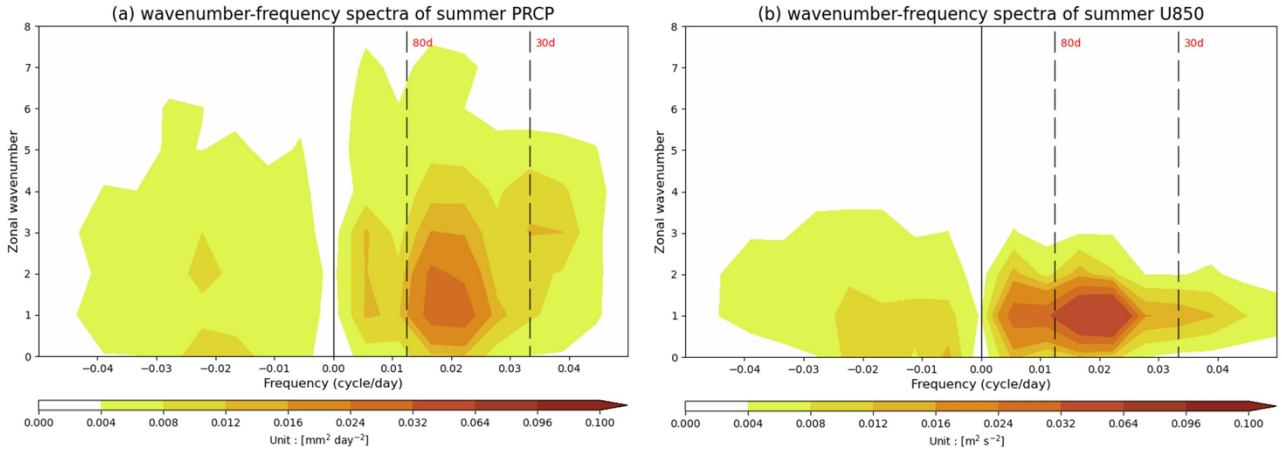

Figure 3 Wavenumber-Frequency spectra of 10°N–10°S meridional mean (a) U850 and (b) PRCP during May-October season.

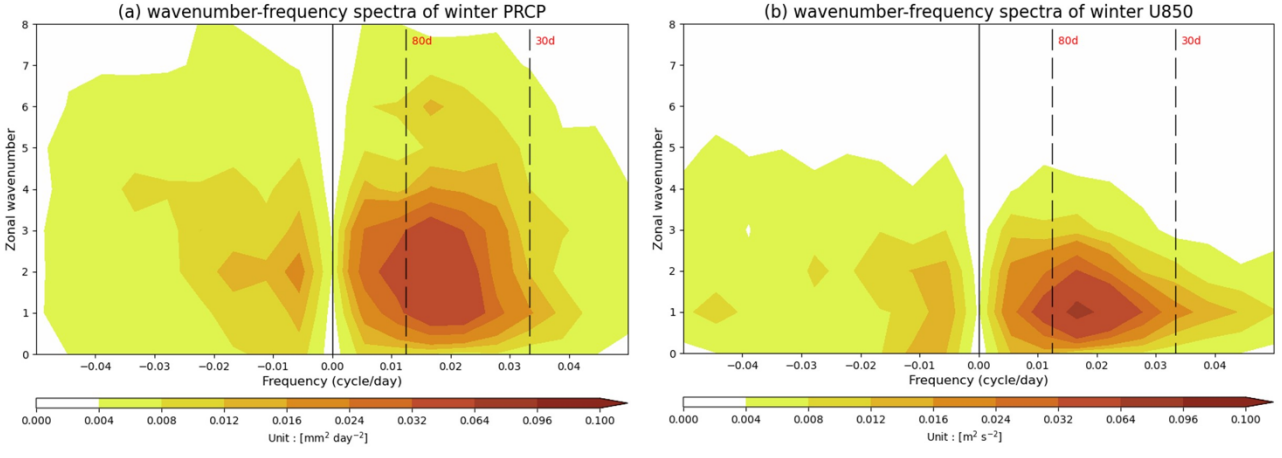

Figure 4 Same as Fig. 3 but for November-April season.

4.2.2 Space–Time Coherence-Squared Spectra and Phase Lag

https://doi.org/10.5194/egusphere-2026-2626
Preprint. Discussion started: 26 May 2026

In this analysis, we use spectral methods to diagnose the space–time scales that cloud activity and zonal winds share. Takayabu (1994) first applied Hayashi's (1971) space–time Fourier analysis to the cloud top brightness temperature data, demonstrating the coupling between tropical waves and convection, and Wheeler and Kiladis (1999) further established the utility of this approach. Here, we calculate coherence spectra between U850 and OLR. By evaluating the phase synchronization between the two variables, the difficulty of estimating background red noise can be avoided (Hendon and Wheeler, 2008). In this analysis, no band-pass filter was applied; the analysis was conducted directly on the daily data.

The calculation method largely follows Hendon and Wheeler (2008). For a variable x(ϕ, θ, t) (in this case, U850 or OLR) that depends on longitude ϕ, latitude θ, and time t, we compute the equatorially symmetric component, x_{symm}, for each date and latitude as

$$x_{\mathrm{symm}}(\phi, |\theta|, t) = \frac{x(\phi, \theta, t) + x(\phi, -\theta, t)}{2}$$

and the equatorially antisymmetric, x_{asym}, component as

$$x_{\mathrm{asym}}(\phi, |\theta|, t) = \frac{x(\phi, \theta, t) - x(\phi, -\theta, t)}{2}$$

where the absolute latitude, |θ|, ranges from 0° to 10°. For each latitude of x_{symm} and x_{asym}, we create segments of 256 days in length, overlapping by 50 days. In the MJO-WG09, the overlap was 206 days but following Hendon and Wheeler (2008) we used 50 days. As a result, for each of x_{symm} and x_{asym}, we obtain three-dimensional datasets covering 0°–360° longitude, 0°–10° absolute latitude, and 256 days, for each segment.

For each segment, we detrend the data in time using linear regression, and apply a cosine-tapered rectangular window of 12 days to set the ends of the segments to zero. For each absolute latitude, we then perform two-dimensional spectral analysis in time and longitude on the 2D time-longitude data for each segment and calculate coherence-squared. At this stage, Hendon and Wheeler (2008) applied a 1–2–1 running filter in the frequency direction to improve visualization; however, we did not apply this filter in the present analysis.

This procedure yields figures similar to Fig. 9 in MJO-WG09 (Appendix A Fig. A5). Although MJO-WG09 does not specify whether a running filter was used, the finer structures visible in Supplementary Fig. A5 suggests that MJO-WG09 likely applied a 1–2–1 running filter. The results indicate that, for MJO-related variability, the OLR minimum leads the U850 maximum by roughly 120° in phase (arrows pointing more to the left), whereas for Kelvin waves, the OLR minimum leads the U850 maximum by roughly 150° (arrows pointing more to the lower left).

4.2.3 Multivariate Combined EOF Modes

https://doi.org/10.5194/egusphere-2026-2626
Preprint. Discussion started: 26 May 2026

Wheeler and Hendon, (2004) first applied multivariate combined empirical orthogonal function (EOF) to MJO diagnostics, and it has since become one of the most widely used methods for identifying the MJO. By jointly analysing OLR—a proxy for convective activity—together with the zonal winds at 200 hPa (U200) and 850 hPa (U850), this method extracts coherent spatial structures in which convection and circulation vary with large amplitudes.

The procedure is as follows. Each variable is first averaged over 15°S–15°N, producing time-longitude fields. A 20-100-day Butterworth band-pass filter is then applied to isolate intraseasonal variability. While Wheeler and Hendon (2004) applied more complex preprocessing and MJO-WG09 employed a Lanczos filter, previous studies have shown that the choice of filter has little influence on the results. Before combining the variables, each is normalized by the square root of the zonal mean of its temporal variance. For each day, the three normalized fields are concatenated along longitude into a single vector. Stacking these vectors over time yields a two-dimensional matrix, from which the variance–covariance matrix, eigenvalues, and eigenvectors are computed. The eigenvectors represent the spatial structures of variability, while the eigenvalues quantify their contributions. The resulting patterns as shown in Fig. 5, closely resemble those in MJO-WG09. However, our results, as well as those of other studies (e.g. Gottschalck et al., 2010; Li et al., 2016), display y-axis values roughly one-tenth those in Wheeler and Hendon (2004) or MJO-WG09. Because neither study provides details of their normalization, we investigated the discrepancy. Examination of the original GrADS scripts revealed that in MJO-WG09, the eigenvectors were scaled by the sample standard deviation of each principal component, effectively rescaling the y-axis to order 10^0 and improving figure readability. Applying this adjustment in our scripts yields figures nearly identical to those in MJO-WG09. In Figs. 5a and 5b we show the unnormalized eigenvectors.

Figure 5c shows the lag correlation between the first and second principal components (PC1 and PC2). The correlation peaks when PC1 leads PC2 by about 10 days and reaches a minimum when PC1 lags by about 10 days, indicating a characteristic period of roughly 40-50 days. Together with the spatial structures of the two leading eigenvectors, the lag correlation between PC1 and PC2 reflects the eastward propagation of convective anomalies from the Indian Ocean to the western Pacific, while the associated large-scale circulation anomalies detach from the convection and circumnavigate the tropics. The strong lag correlation further supports the interpretation that PC1 and PC2 together provide a meaningful two-dimensional phase-space representation of the MJO, as demonstrated by Wheeler and Hendon (2004). We also note that Fig. 5c closely matches the corresponding figure in MJO-WG09.

Figure 5d shows the spectral analysis of a one-dimensional time series obtained by projecting the time-longitude fields onto the leading EOF modes. These time-longitude fields were constructed in a similar way as for the

https://doi.org/10.5194/egusphere-2026-2626
Preprint. Discussion started: 26 May 2026

preceding EOF analysis: the three variables of U200, U850, and OLR were combined after normalizing each by the square root of the zonal mean of its temporal variance, but no temporal filtering was applied. Note that Fig. 5d required detailed examination and several modifications from MJO-WG09. We therefore summarize below the procedures used to construct the PC1 time series for spectral analysis.

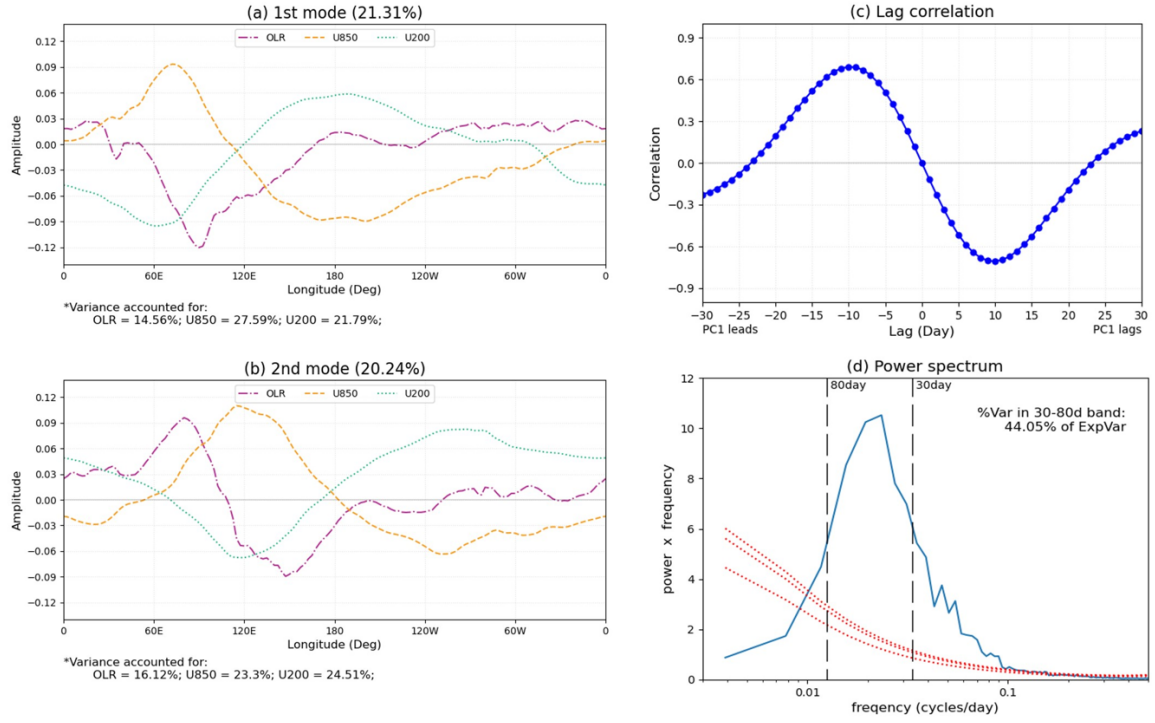

Figure 5 (a) 1st and (b) 2nd modes of unnormalized eigenvectors, (c) lag correlation between first two principal components of combined EOF of intraseasonal-filtered OLR, U850 and U200, and (d) power spectrum of PC1 calculated as projection of the first EOF to the unfiltered time series of OLR, U850 and U200 normalized by the square root of their respective zonal mean variance. Red lines in (d) show the red noise spectrum and upper 90% and 95% confidence limits on this red noise spectrum.

In this analysis, MJO-WG09 followed the approach of Maloney and Hartmann (1998), who projected unfiltered U200 anomalies onto EOF modes derived from filtered U200 fields. Extending this method to combined fields of OLR, U850, and U200, however, causes OLR to dominate the resulting PC1. To address this, we constructed the PC1 time series by projecting the leading combined EOF of OLR, U850, and U200 (as computed in the previous

https://doi.org/10.5194/egusphere-2026-2626
Preprint. Discussion started: 26 May 2026

analysis) onto one-dimensional vectors formed from unfiltered anomalies of the three variables, each normalized by the square root of its zonal mean variance. This normalization prevents OLR from overwhelming the signal.

We next summarize the differences in spectral analysis methods. In our Fig. 5d, the vertical axis range is about one-tenth of that shown in MJO-WG09, and other studies performing similar analyses report yet different scales (e.g., Li et al., 2016; Wheeler and Hendon, 2004). These discrepancies appear to arise from details of the spectral formulation. Inspection of the original MJO-WG09 Fortran implementation shows that the function $f(t)$ is represented using the real discrete Fourier transformation (DFT) by:

$$f(t) = a_0 + \sum_{k=1}^{N/2} \left[a_k \cos\left(\frac{2\pi kt}{N\Delta t}\right) + b_k \sin\left(\frac{2\pi kt}{N\Delta t}\right) \right]$$

where N denotes the length of the time series and Δt is the sampling interval. The coefficients a_k and b_k denote the cosine and sine Fourier coefficients, respectively, and are computed as

$$a_k = \frac{2}{N} \sum_{n=0}^{N-1} f(t_n) \cos\left(\frac{2\pi kn}{N}\right)$$

$$b_k = \frac{2}{N} \sum_{n=0}^{N-1} f(t_n) \sin\left(\frac{2\pi kn}{N}\right)$$

with $t_n = n\Delta t$.

The associated power spectrum, P_k, is defined as

$$P_k = \frac{a_k^2 + b_k^2}{2}$$

Repeating the analysis with this formulation yielded spectra of $P_k \frac{2\pi}{N\Delta t} kt$ (i.e., power × frequency, following Zangvil, 1977) comparable to those in the original study. In contrast, our Python implementation employs the standard complex-valued convention adopted in NumPy—specifically numpy.fft.fft for the DFT and numpy.abs for amplitude conversion. Here, forward DFT in NumPy is defined as

$$F_k = \sum_{n=0}^{N-1} f(t_n) e^{-i\frac{2\pi}{N}kn}, \qquad k = 0, \ldots, N-1$$

and the corresponding power, P'_k, is defined as

https://doi.org/10.5194/egusphere-2026-2626
Preprint. Discussion started: 26 May 2026

$$P'_k = \frac{|F_k|^2}{N}$$

Because $|F_k|^2 = \Re(F_k)^2 + \Im(F_k)^2$ the NumPy coefficients can be related to the real Fourier-series coefficients via $a_k = \frac{2}{N}\Re(F_k)$ and $b_k = -\frac{2}{N}\Im(F_k)$. Substituting these into the real-series expression shows that P_k is related to P'_k by $P_k = P'_k \frac{N}{2}$.

Given the wide adoption of Python libraries across disciplines, and the advantages of adhering to a broadly used and standardized approach, we consider this update to the spectral analysis method to be reasonable.

4.2.4 Life Cycle Composites

Since its introduction by Wheeler and Hendon (2004), this analysis has become a widely used method for depicting the characteristic horizontal structures of the MJO and their temporal evolution. By grouping days when convection and circulation are in similar states, composite analysis can illustrate the eastward propagation of convective activity, atmospheric circulation, and surface conditions. Using the PC1 and PC2 time series obtained in Section 4.2d, we calculate the daily coordinates (PC1′, PC2′), with the phase definition following Wheeler and Hendon (2004). Appendix A Figs. A6 and A7 show composites of intraseasonal (20-100 days) anomalies of 10 m vectors (U_{10m}, V_{10m}) and PRCP for boreal summer and winter, respectively, while Appendix A Figs. A8 and A9 show composites of intraseasonal (20-100 days) anomalies of SST and PRCP for the two seasons. These results closely resemble Figs. 11–14 of MJO-WG09.

MJO-WG09 stated that only surface wind vectors at the 99% significance level were plotted. However, inspection of the distributed Fortran code revealed that no such statistical test was implemented. Given the variability of MJO behaviour, it is also unlikely that many grid points would meet the 99% threshold. Indeed, when we attempted to plot only vectors at the 99% level, very few points were retained, producing results that differed substantially from the original figures. For this reason, our program does not apply a significance test when plotting the wind vectors.

4.2.5 Mean Walker Circulation

This diagnostic was not included in the MJO-WG09. However, recent work suggests that the large-scale zonal circulation of the atmosphere on timescales longer than the MJO itself can strongly influence the ability of GCRMs/GSRMs to realistically simulate the MJO (Suematsu et al. 2022). Takasuka et al. (2021) further showed that the descending branch of the Walker circulation over the Indian Ocean is associated with a shortening of the

https://doi.org/10.5194/egusphere-2026-2626
Preprint. Discussion started: 26 May 2026

wavelength of mixed Rossby waves, leading to eastward and downward radiation of wave energy that can trigger the MJO. For these reasons, we propose this analysis as a new standard diagnostic for evaluating the link between a model's representation of the Walker circulation and its fidelity in simulating the MJO.

We use zonal wind (U) and vertical velocity (ω). For each day, full 3D fields spanning 0–360° longitude are processed. Within the latitude band of 15°S–15°N, we compute an area-weighted meridional mean. The daily data are then divided into boreal summer and boreal winter segments, and seasonal means are calculated for each.

Figs. 6a and 6b illustrate the resulting Walker circulation during boreal summer and winter, respectively. The region from the Indian Ocean to the central Pacific, where MJO convective activity is typically observed, is characterized by negative ω values, indicating climatological ascent. In both seasons, the strongest upward motion is located approximately 150°E. West of this maximum, the lower troposphere is dominated by westerlies and the upper troposphere by easterlies, while the opposite pattern occurs to the east—lower-tropospheric easterlies and upper-tropospheric westerlies. During boreal summer, the ascent tends to split between the Indian Ocean and the western Pacific, reflecting the dry season over the Maritime Continent. In boreal winter, the lower-tropospheric subsidence around 130°E weakens considerably, creating a background state more favourable for MJO passage across the Maritime Continent (Figs. 7a and 7b).

An interesting feature common to both seasons is the strong, narrow subsidence near 50°E, with a longitudinal width of approximately 20°. As discussed by Kohyama et al. (2021), this "wall" of descent is likely linked to orographic gravity waves generated over Africa. The associated convergence of zonal winds aloft forms a coupled structure with this subsidence, providing a background state that distorts the horizontal scale of MRG waves (Aiyyer and Molinari, 2003) and facilitates eastward radiation of wave energy (Takasuka et al., 2021). The magnitudes of both the subsidence and the zonal convergence are stronger in boreal summer than in boreal winter.

https://doi.org/10.5194/egusphere-2026-2626
Preprint. Discussion started: 26 May 2026

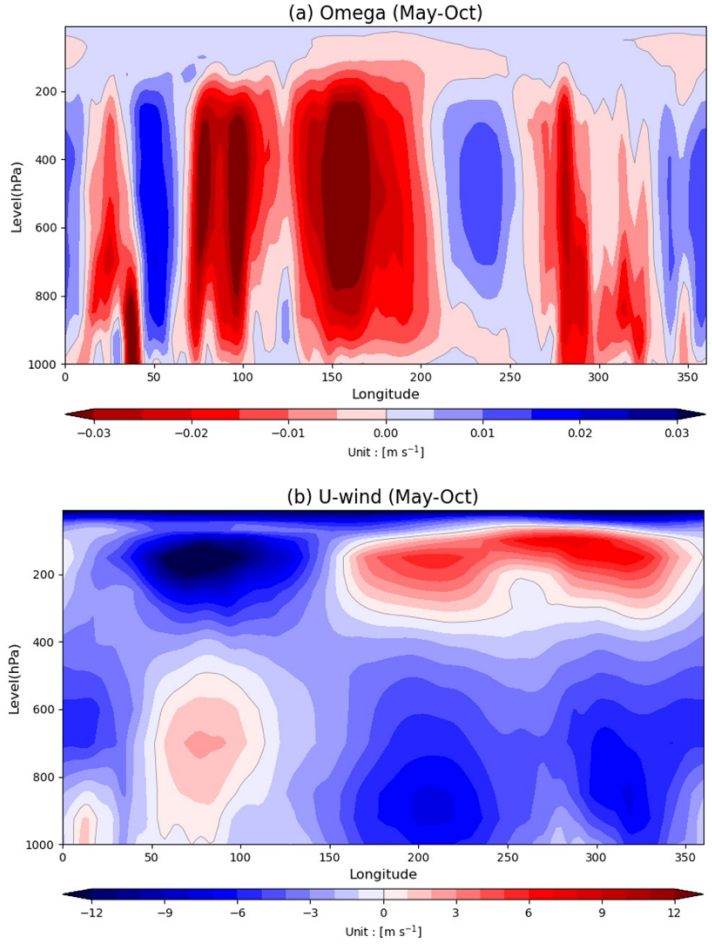

375 **Figure 6** 15°S–15°N meridionally averaged May-October mean (a) ω and (b) U.

https://doi.org/10.5194/egusphere-2026-2626
Preprint. Discussion started: 26 May 2026

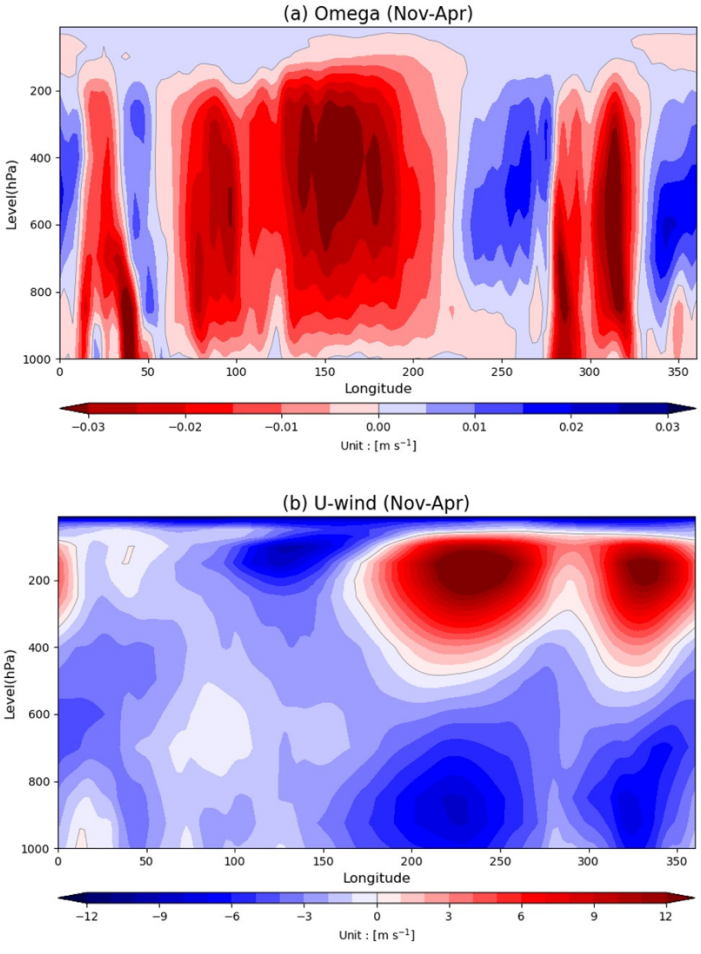

Figure 7 Same as Fig. 6 but for Nov-April season.

5. Summary

Despite initial expectations, the reproducibility of the MJO has not markedly improved even in high-resolution GCRM/GSRM simulations. At the same time, seasonal-scale predictions using AI models are beginning to emerge. Because the MJO is often regarded as a key source of predictability on subseasonal timescales—particularly for midlatitude forecasts on the order of one month—there is clear value in evaluating traditional GCMs, high-resolution GCRM/GSRMs, and AI-based models within a common diagnostic framework. Such comparisons can advance both model development and the physical understanding of the MJO.

https://doi.org/10.5194/egusphere-2026-2626
Preprint. Discussion started: 26 May 2026

As a first step toward a unified evaluation platform, we updated diagnostic methods originally proposed more than a decade ago but now difficult to access. Specifically, we reimplemented the MJO Diagnostics package by MJO-WG09 —formerly distributed in Fortran and GrADS—using modern Python libraries. With the original website no longer available and the legacy code hard to obtain, our Python programs provide a practical substitute. The updated package is available at https://zenodo.org/records/19563199.

The programs presented here are not entirely new but represent a reorganization of well-established diagnostics from the original MJO Diagnostics framework. They remain valuable tools; yet more complex analyses are now needed than those envisioned fifteen years ago (see Jiang et al., 2021 for a review on the process-oriented MJO diagnostics). An example is the moist static energy and moisture budget analysis (Maloney, 2009; Ren et al., 2021) which has been widely used to understand the dynamics of the MJO in observations (e.g. Kim et al., 2014, 2017) and model simulations (e.g. Ahn et al., 2020b; Chikira and Sugiyama, 2013; Jiang, 2017). Also, it has become increasingly important to compare MJO-related teleconnections in the midlatitudes across models (Stan et al., 2025). There is also evidence that some models may overestimate air–sea coupling (Chen et al., 2020), and recent studies highlight the role of the background SST state in sustaining the MJO (e.g., Suematsu and Miura 2018, Takano et al., 2024). Future assessments will therefore need to explicitly evaluate oceanic influences.

Research has also expanded toward understanding MJO diversity (Wang et al., 2019). Analyses are evolving from relatively simple approaches that identify eastward-propagating large-scale cloud systems, toward more sophisticated tracking of individual cloud systems embedded within the MJO (e.g., Feng et al., 2023; Kerns and Chen, 2016; Suematsu and Miura, 2022).

Finally, developing diagnostic tools also raises the need to reconsider how the MJO itself is defined, as no universally accepted definition currently exists. While unifying diagnostic approaches into a single framework is beyond the scope of any one group, efforts such as ours—re-establishing and maintaining standard diagnostics and making them widely accessible—remain essential for advancing MJO research and improving climate models.

Acknowledgement

We thank Yuta Kawai and Tomoro Yanase for the initial quality check of the python codes implemented in this work. This work has been supported by JSPS-Kakenhi 23K2539 and 21K13991, National Research Foundation of Korea (NRF) grant funded by the Korea government (MSIT) (RS-2024-00336160), and the Korea Meteorological Administration Research and Development Program under Grant (RS-2025-02221669). The quality check was conducted using supercomputer FUGAKU at RIKEN Center for Computational Science (Proposal number ra000005). This study builds upon the MJO diagnostic tools developed by Waliser et al. (2009). We encourage

https://doi.org/10.5194/egusphere-2026-2626
Preprint. Discussion started: 26 May 2026

readers to cite Waliser et al. (2009) alongside the present work when relevant. ChatGPT was used to improve the readability of the manuscript.

Code and data availability

The MJO diagnostic package described in this paper is implemented in Python and made publicly available via Zenodo (https://zenodo.org/records/19563199). A versioned release of the code corresponding to this manuscript will be archived on Zenodo and assigned a DOI of 10.5281/zenodo.19563199. All datasets used in this work are publicly available and are referenced in the main text. No new observational or model datasets were generated specifically for this study.

References

Ahn, M. S., Kim, D., Kang, D., Lee, J., Sperber, K. R., Gleckler, P. J., Jiang, X., Ham, Y. G., and Kim, H.: MJO Propagation Across the Maritime Continent: Are CMIP6 Models Better Than CMIP5 Models?, Geophys. Res. Lett., 47, e2020GL087250, https://doi.org/10.1029/2020GL087250, 2020a.

Aiyyer And, A. R. and Molinari, J.: Evolution of Mixed Rossby-Gravity Waves in Idealized MJO Environments, J. Atmos. Sci., 60, 2387–2855, https://doi.org/doi.org/10.1175/1520-0469(2003)060<2837:EOMRWI>2.0.CO;2., 2003.

Chen, G., Ling, J., Li, C., Zhang, Y., and Zhang, C.: Barrier effect of the indo-pacific maritime continent on MJO propagation in observations and CMIP5 models, J. Clim., 33, 5173–5193, https://doi.org/10.1175/JCLI-D-19-0771.1, 2020.

Chikira, M. and Sugiyama, M.: Eastward-Propagating Intraseasonal Oscillation Represented by Chikira–Sugiyama Cumulus Parameterization. Part I: Comparison with Observation and Reanalysis, J. Atmos. Sci., 70, 3920–3939, https://doi.org/10.1175/JAS-D-13-034.1, 2013.

Feng, Z., Hardin, J., Barnes, H. C., Li, J., Leung, L. R., Varble, A., and Zhang, Z.: PyFLEXTRKR: a flexible feature tracking Python software for convective cloud analysis, Geosci. Model Dev., 16, 2753–2776, https://doi.org/10.5194/GMD-16-2753-2023, 2023.

Gottschalck, J., Wheeler, M., Weickmann, K., Vitart, F., Savage, N., Lin, H., Hendon, H., Waliser, D., Sperber, K., Nakagawa, M., Prestrelo, C., Flatau, M., and Higgins, W.: A Framework for Assessing Operational Madden–Julian Oscillation Forecasts: A CLIVAR MJO Working Group Project, Bull. Am. Meteorol. Soc., 91, 1247–1258, https://doi.org/10.1175/2010BAMS2816.1, 2010.

Hayashi, Y.: A Generalized Method of Resolving Disturbances into Progressive and Retrogressive Waves by Space Fourier and Time Cross-Spectral Analyses, Journal of the Meteorological Society of Japan. Ser. II, 49, 125–128, https://doi.org/10.2151/JMSJ1965.49.2_125, 1971.

Hendon, H. H. and Wheeler, M. C.: Some Space–Time Spectral Analyses of Tropical Convection and Planetary-Scale Waves, J. Atmos. Sci., 65, 2936–2948, https://doi.org/10.1175/2008JAS2675.1, 2008.

https://doi.org/10.5194/egusphere-2026-2626
Preprint. Discussion started: 26 May 2026

Huang, B., Liu, C., Banzon, V., Freeman, E., Graham, G., Hankins, B., Smith, T., and Zhang, H. M.: Improvements of the Daily Optimum Interpolation Sea Surface Temperature (DOISST) Version 2.1, J. Clim., 34, 2923–2939, https://doi.org/10.1175/JCLI-D-20-0166.1, 2021.

Hung, M. P., Lin, J. L., Wang, W., Kim, D., Shinoda, T., and Weaver, S. J.: MJO and Convectively Coupled Equatorial Waves Simulated by CMIP5 Climate Models, J. Clim., 26, 6185–6214, https://doi.org/10.1175/JCLI-D-12-00541.1, 2013.

Jiang, X.: Key processes for the eastward propagation of the Madden-Julian Oscillation based on multimodel simulations, Journal of Geophysical Research: Atmospheres, 122, 755–770, https://doi.org/10.1002/2016JD025955, 2017.

Jiang, X., Adames, Á. F., Kim, D., Maloney, E. D., Lin, H., Kim, H., Zhang, C., DeMott, C. A., and Klingaman, N. P.: Fifty Years of Research on the Madden-Julian Oscillation: Recent Progress, Challenges, and Perspectives, Journal of Geophysical Research: Atmospheres, 125, e2019JD030911, https://doi.org/10.1029/2019JD030911, 2020.

Jiang, X., Kim, D., and Maloney, E. D.: Progress and Status of MJO Simulation in Climate Models and Process-Oriented Diagnostics, World Scientific Series on Asia-Pacific Weather and Climate, 11, 315–326, https://doi.org/10.1142/9789811216602_0025, 2021.

Kanamitsu, M., Ebisuzaki, W., Woollen, J., Yang, S.-K., Hnilo, J. J., Fiorino, M., Potter, G. L., Kanamitsu, M., Ebisuzaki, W., Woollen, J., Yang, S.-K., Hnilo, J. J., Fiorino, M., and Potter, G. L.: NCEP–DOE AMIP-II Reanalysis (R-2), Bull. Am. Meteorol. Soc., 83, 1631–1644, https://doi.org/10.1175/BAMS-83-11-1631, 2002.

Kerns, B. W. and Chen, S. S.: Large-scale precipitation tracking and the MJO over the Maritime Continent and Indo-Pacific warm pool, Journal of Geophysical Research: Atmospheres, 121, 8755–8776, https://doi.org/10.1002/2015JD024661, 2016.

Kim, D. and Maloney, E. D.: Simulation of the madden-julian oscillation using general circulation models, World Scientific Series on Asia-Pacific Weather and Climate, Volume 9, 119–130, https://doi.org/10.1142/9789813200913_0009, 2017.

Kim, D., Sperber, K., Stern, W., Waliser, D., Kang, I. S., Maloney, E., Wang, W., Weickmann, K., Benedict, J., Khairoutdinov, M., Lee, M. I., Neale, R., Suarez, M., Thayer-Calder, K., and Zhang, G.: Application of MJO Simulation Diagnostics to Climate Models, J. Clim., 22, 6413–6436, https://doi.org/10.1175/2009JCLI3063.1, 2009.

Kim, D., Kug, J. S., and Sobel, A. H.: Propagating versus nonpropagating Madden-Julian oscillation events, J. Clim., 27, 111–125, https://doi.org/10.1175/JCLI-D-13-00084.1, 2014.

Kim, D., Kim, H., and Lee, M. I.: Why does the MJO detour the Maritime Continent during austral summer?, Geophys. Res. Lett., 44, 2579–2587, https://doi.org/10.1002/2017GL072643, 2017.

Kochkov, D., Yuval, J., Langmore, I., Norgaard, P., Smith, J., Mooers, G., Klöwer, M., Lottes, J., Rasp, S., Düben, P., Hatfield, S., Battaglia, P., Sanchez-Gonzalez, A., Willson, M., Brenner, M. P., and Hoyer, S.: Neural general circulation models for weather and climate, Nature 2024 632:8027, 632, 1060–1066, https://doi.org/10.1038/s41586-024-07744-y, 2024.

Lam, R., Sanchez-Gonzalez, A., Willson, M., Wirnsberger, P., Fortunato, M., Alet, F., Ravuri, S., Ewalds, T., Eaton-Rosen, Z., Hu, W., Merose, A., Hoyer, S., Holland, G., Vinyals, O., Stott, J., Pritzel, A., Mohamed, S., and Battaglia, P.: Learning skillful medium-range global weather forecasting, Science (1979)., 382, 1416–1422, https://doi.org/10.1126/SCIENCE.ADI2336/SUPPL_FILE/SCIENCE.ADI2336_SM.PDF, 2023.

https://doi.org/10.5194/egusphere-2026-2626
Preprint. Discussion started: 26 May 2026

Li, X., Tang, Y., Zhou, L., Chen, D., Yao, Z., and Islam, S. U.: Assessment of Madden–Julian oscillation simulations with various configurations of CESM, Clim. Dyn., 47, 2667–2690, https://doi.org/10.1007/S00382-016-2991-0/FIGURES/16, 2016.

Liebmann, B. and Smith, C.: Description of a complete (interpolated) outgoing longwave radiation dataset, Bull. Amer. Met. Soc., 77, 1275–1277, 1996.

Lin, J. L., Kiladis, G. N., Mapes, B. E., Weickmann, K. M., Sperber, K. R., Lin, W., Wheeler, M. C., Schubert, S. D., Del Genio, A., Donner, L. J., Emori, S., Gueremy, J. F., Hourdin, F., Rasch, P. J., Roeckner, E., and Scinocca, J. F.: Tropical Intraseasonal Variability in 14 IPCC AR4 Climate Models. Part I: Convective Signals, J. Clim., 19, 2665–2690, https://doi.org/10.1175/JCLI3735.1, 2006.

Madden, R. A. and Julian, P. R.: Detection of a 40–50 Day Oscillation in the Zonal Wind in the Tropical Pacific, J. Atmos. Sci., 28, 702–708, https://doi.org/10.1175/1520-0469(1971)028<0702:DOADOI>2.0.CO;2, 1971.

Madden, R. A. and Julian, P. R.: Description of Global-Scale Circulation Cells in the Tropics with a 40–50 Day Period, J. Atmos. Sci., 29, 1109–1123, https://doi.org/10.1175/1520-0469(1972)029<1109:DOGSCC>2.0.CO;2, 1972.

Maloney, E. D.: The Moist Static Energy Budget of a Composite Tropical Intraseasonal Oscillation in a Climate Model, J. Clim., 22, 711–729, https://doi.org/10.1175/2008JCLI2542.1, 2009.

Maloney, E. D. and Hartmann, D. L.: Frictional Moisture Convergence in a Composite Life Cycle of the Madden-Julian Oscillation, J. Clim., 11, 2387–2403, https://doi.org/doi.org/10.1175/1520-0442(1998)011<2387:FMCIAC>2.0.CO;2., 1998.

Miura, H.: Difficulties in the Subgrid-Scale Redistribution of Moisture of a Global Cloud-Resolving Model, 207–217, https://doi.org/10.1007/978-981-13-3396-5_11, 2019.

Miura, H., Satoh, M., Nasuno, T., Noda, A. T., and Oouchi, K.: A Madden-Julian Oscillation Event Realistically Simulated by a Global Cloud-Resolving Model, Science (1979)., 318, 1763–1765, https://doi.org/10.1126/science.1148443, 2007.

Price, I., Sanchez-Gonzalez, A., Alet, F., Andersson, T. R., El-Kadi, A., Masters, D., Ewalds, T., Stott, J., Mohamed, S., Battaglia, P., Lam, R., and Willson, M.: Probabilistic weather forecasting with machine learning, Nature 2024 637:8044, 637, 84–90, https://doi.org/10.1038/s41586-024-08252-9, 2024.

Ren, P., Kim, D., Ahn, M. S., Kang, D., and Ren, H. L.: Intercomparison of MJO Column Moist Static Energy and Water Vapor Budget among Six Modern Reanalysis Products, J. Clim., 34, 2977–3001, https://doi.org/10.1175/JCLI-D-20-0653.1, 2021.

Slingo, J. M.: Intraseasonal oscillation in 15 atmospheric general circulation models: results from an AMIP diagnostic subproject, Clim. Dyn., 12, 325–357, https://doi.org/10.1007/BF00231106/METRICS, 1996.

Stan, C., Kollapaneni, S., Jenney, A. M., Wang, J., Wu, Z., Zheng, C., Kim, H., Garfinkel, C. I., and Singh, A.: A Python diagnostics package for evaluation of Madden-Julian Oscillation (MJO) teleconnections in subseasonal-To-seasonal (S2S) forecast systems, Geosci. Model Dev., 18, 7969–7985, https://doi.org/10.5194/GMD-18-7969-2025, 2025.

Suematsu, T. and Miura, H.: Zonal SST Difference as a Potential Environmental Factor Supporting the Longevity of the Madden–Julian Oscillation, J. Clim., 31, 7549–7564, https://doi.org/10.1175/JCLI-D-17-0822.1, 2018.

https://doi.org/10.5194/egusphere-2026-2626
Preprint. Discussion started: 26 May 2026

Suematsu, T. and Miura, H.: Changes in the Eastward Movement Speed of the Madden–Julian Oscillation with Fluctuation in the Walker Circulation, J. Clim., 35, 211–225, https://doi.org/10.1175/JCLI-D-21-0269.1, 2022.

Suematsu, T., Miura, H., Kodama, C., and Takasuka, D.: Deceleration of Madden–Julian Oscillation Speed in NICAM AMIP-Type Simulation Associated With Biases in the Walker Circulation Strength, Geophys. Res. Lett., 49, e2022GL098628, https://doi.org/10.1029/2022GL098628, 2022.

Takano, Y. H., Kodama, C., and Miura, H.: Diagnostic Method for Atmosphere–Ocean Coupling Over Tropical Oceans at the Sub-Seasonal Timescale, Geophys. Res. Lett., 51, e2023GL106837, https://doi.org/10.1029/2023GL106837, 2024.

Takasuka, D., Kohyama, T., Miura, H., and Suematsu, T.: MJO Initiation Triggered by Amplification of Upper-Tropospheric Dry Mixed Rossby-Gravity Waves, Geophys. Res. Lett., 48, e2021GL094239, https://doi.org/10.1029/2021GL094239, 2021.

Takasuka, D., Kodama, C., Suematsu, T., Ohno, T., Yamada, Y., Seiki, T., Yashiro, H., Nakano, M., Miura, H., Noda, A. T., Nasuno, T., Miyakawa, T., and Masunaga, R.: How Can We Improve the Seamless Representation of Climatological Statistics and Weather Toward Reliable Global K-Scale Climate Simulations?, J. Adv. Model. Earth Syst., 16, e2023MS003701, https://doi.org/10.1029/2023MS003701, 2024.

Takayabu, Y. N.: Large-Scale Cloud Disturbances Associated with Equatorial Waves, Journal of the Meteorological Society of Japan. Ser. II, 72, 433–449, 1994.

Waliser, D., Sperber, K., Hendon, H., Kim, D., Maloney, E., Wheeler, M., Weickmann, K., Zhang, C., Donner, L., Gottschalck, J., Higgins, W., Kang, I. S., Legler, D., Moncrieff, M., Schubert, S., Stern, W., Vitart, F., Wang, B., Wang, W., and Woolnough, S.: MJO Simulation Diagnostics, J. Clim., 22, 3006–3030, https://doi.org/10.1175/2008JCLI2731.1, 2009.

Wang, B. and Rui, H.: Synoptic climatology of transient tropical intraseasonal convection anomalies: 1975–1985, Meteorology and Atmospheric Physics, 44, 43–61, https://doi.org/10.1007/BF01026810, 1990.

Wang, B., Chen, G., and Liu, F.: Diversity of the Madden-Julian Oscillation, Sci. Adv., 5, eaax0220, https://doi.org/10.1126/sciadv.aax0220, 2019.

Wheeler, M. and Kiladis, G. N.: Convectively Coupled Equatorial Waves: Analysis of Clouds and Temperature in the Wavenumber–Frequency Domain, J. Atmos. Sci., 56, 374–399, https://doi.org/10.1175/1520-0469(1999)056<0374:CCEWAO>2.0.CO;2, 1999.

Wheeler, M. C. and Hendon, H. H.: An All-Season Real-Time Multivariate MJO Index: Development of an Index for Monitoring and Prediction, Mon. Weather Rev., 132, 1917–1932, https://doi.org/10.1175/1520-0493(2004)132<1917:AARMMI>2.0.CO;2, 2004.

Xie, P. and Arkin, P. A.: Global Precipitation: A 17-Year Monthly Analysis Based on Gauge Observations, Satellite Estimates, and Numerical Model Outputs, Bull. Am. Meteorol. Soc., 78, 2539–2558, https://doi.org/https://doi.org/10.1175/1520-0477(1997)078%3C2539:GPAYMA%3E2.0.CO;2, 1997.

Yasunari, T.: Cloudiness Fluctuations Associated with the Northern Hemisphere Summer Monsoon, Journal of the Meteorological Society of Japan. Ser. II, 57, 227–242, https://doi.org/10.2151/JMSJ1965.57.3_227, 1979.

https://doi.org/10.5194/egusphere-2026-2626
Preprint. Discussion started: 26 May 2026

Zangvil, A.: On the Presentation and interpretation of spectra of large-scale disturbances, Mon Weather Rev, 105, 1469–1472, https://doi.org/https://doi.org/10.1175/1520-0493(1977)105<1469:OTPAIO>2.0.CO;2, 1977.

https://doi.org/10.5194/egusphere-2026-2626
Preprint. Discussion started: 26 May 2026

560

Appendix A Additional figures and captions

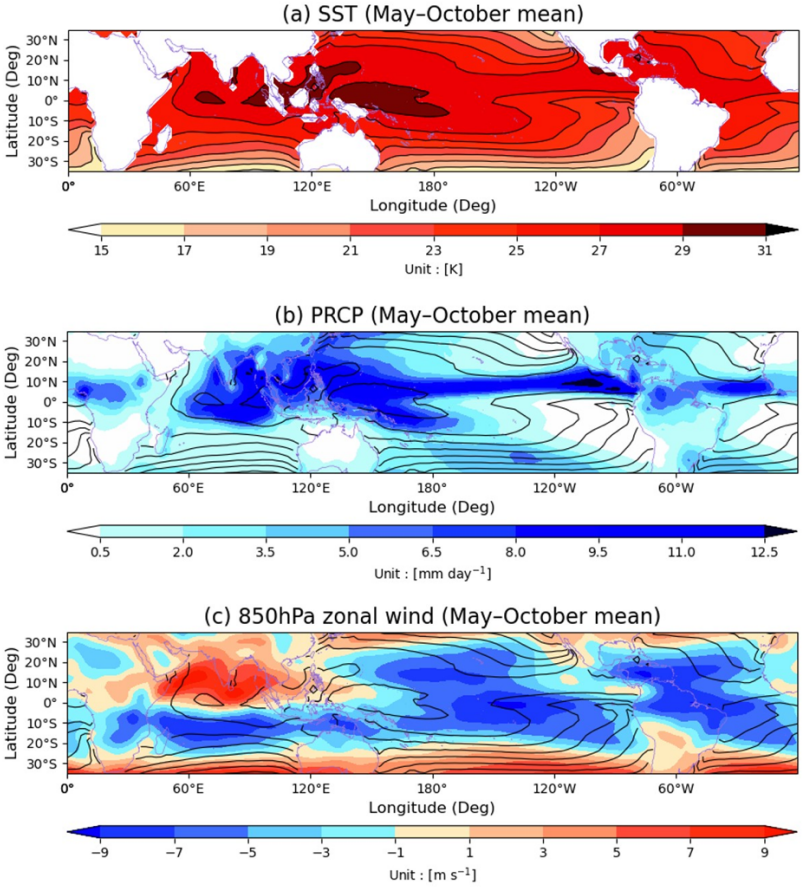

Figure A1 May-October mean (a) SST (shades), (b) PRCP (shades) and (c) U850 (shades). Contours indicate
565 SST in all panels.

https://doi.org/10.5194/egusphere-2026-2626
Preprint. Discussion started: 26 May 2026

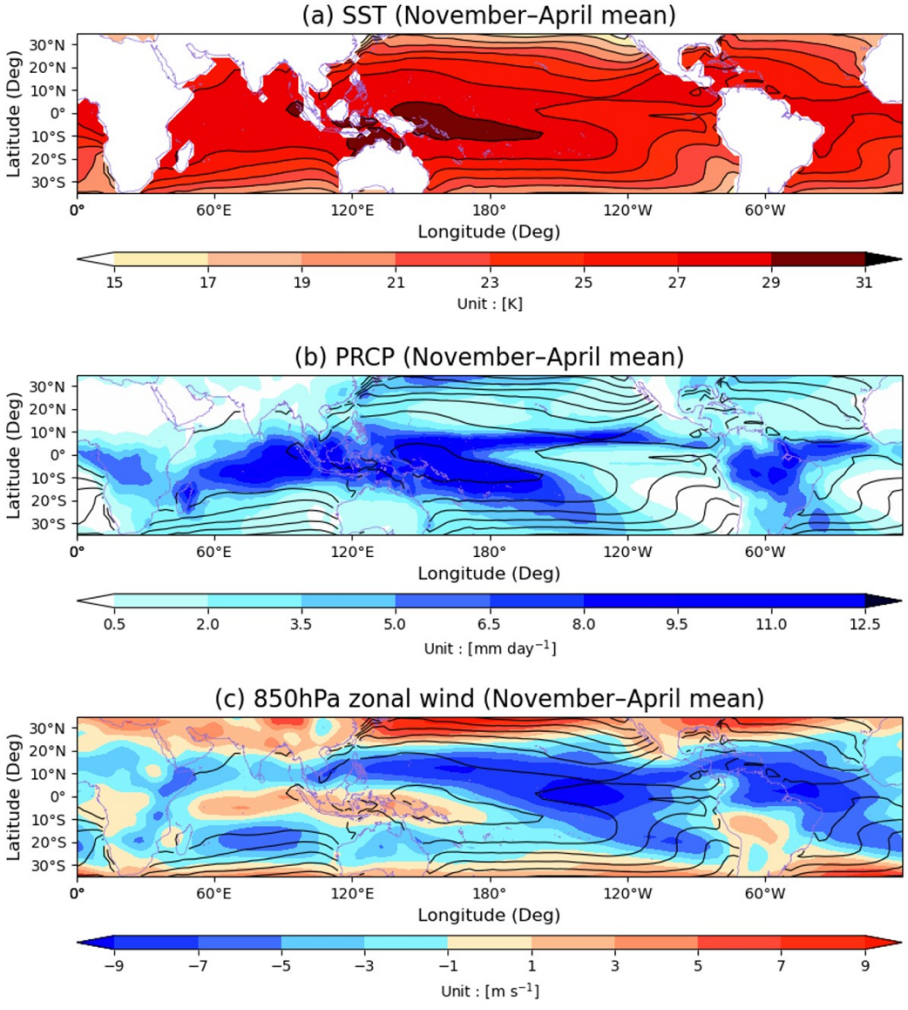

570 **Figure A2** As in Fig. A1 but for November-April season.

https://doi.org/10.5194/egusphere-2026-2626
Preprint. Discussion started: 26 May 2026

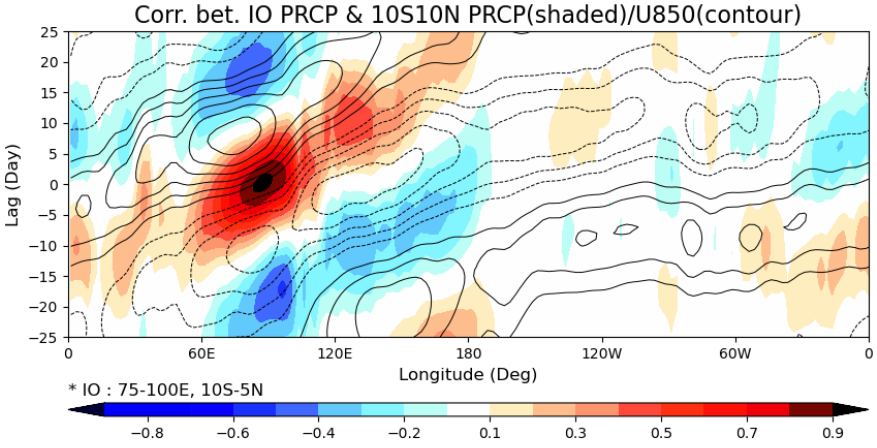

Figure A3 Lag-longitude correlation of intraseasonal (20-100 days) 10°N–10°S mean PRCP (shades) and U850 (contours) to area averaged PRCP over Indian Ocean region (5°N–10°S, 75°E–100°E).

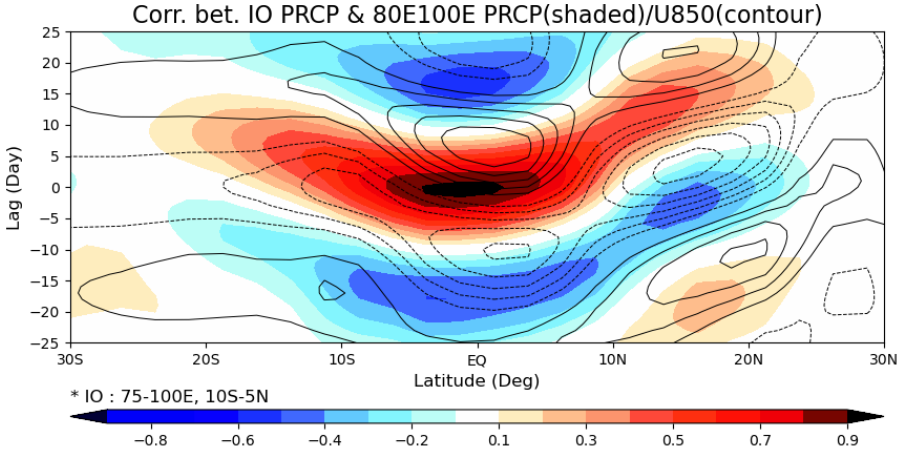

Figure A4 Lag-latitude correlation of intraseasonal (20-100 days) 80°E–100°E mean PRCP (shades) and U850 (contours) to area averaged PRCP over Indian Ocean region (5°N–10°S, 75°E–100°E).

https://doi.org/10.5194/egusphere-2026-2626
Preprint. Discussion started: 26 May 2026

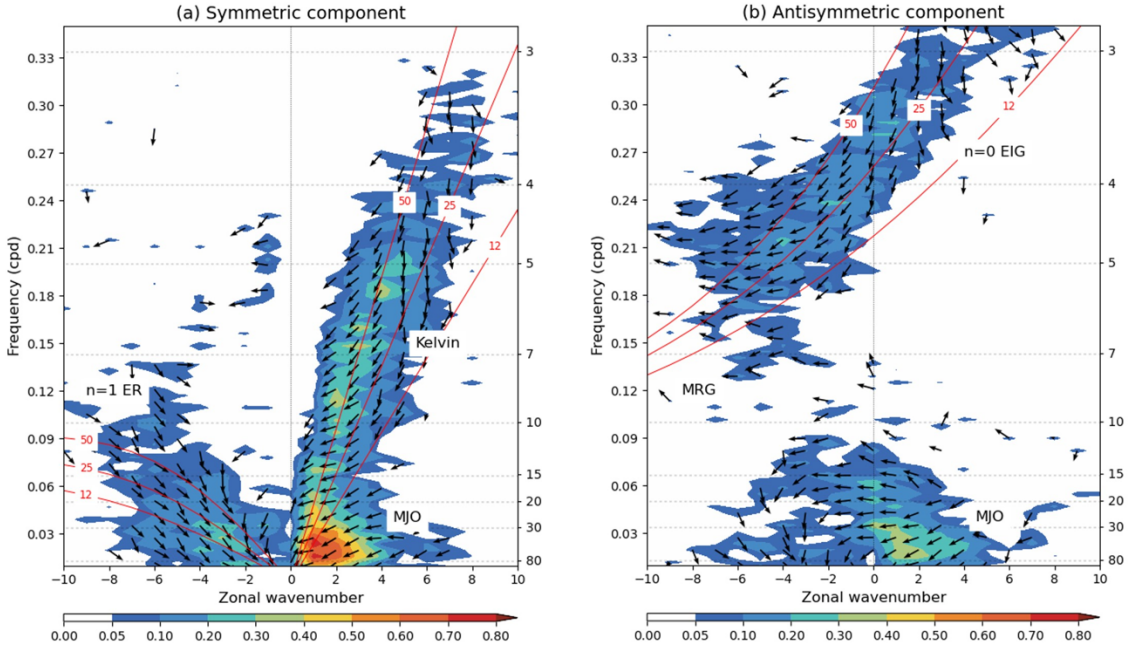

Figure A5 Coherence squared (colors) and phase lag (vectors) between (a) symmetric and (b) asymmetric components of OLR and U850. Vectors of the phase lags are oriented so that phase of 0° is represented by an upward vector. Dispersion relations for n=-1 Kelvin, n=1 equatorial Rossby (ER), n=0 eastward inertia gravity waves (EIG), and mixed Rossby-gravity modes corresponding to equivalent depths of 12, 25 and 50m in shallow water equations are overlaid (red contours).

https://doi.org/10.5194/egusphere-2026-2626
Preprint. Discussion started: 26 May 2026

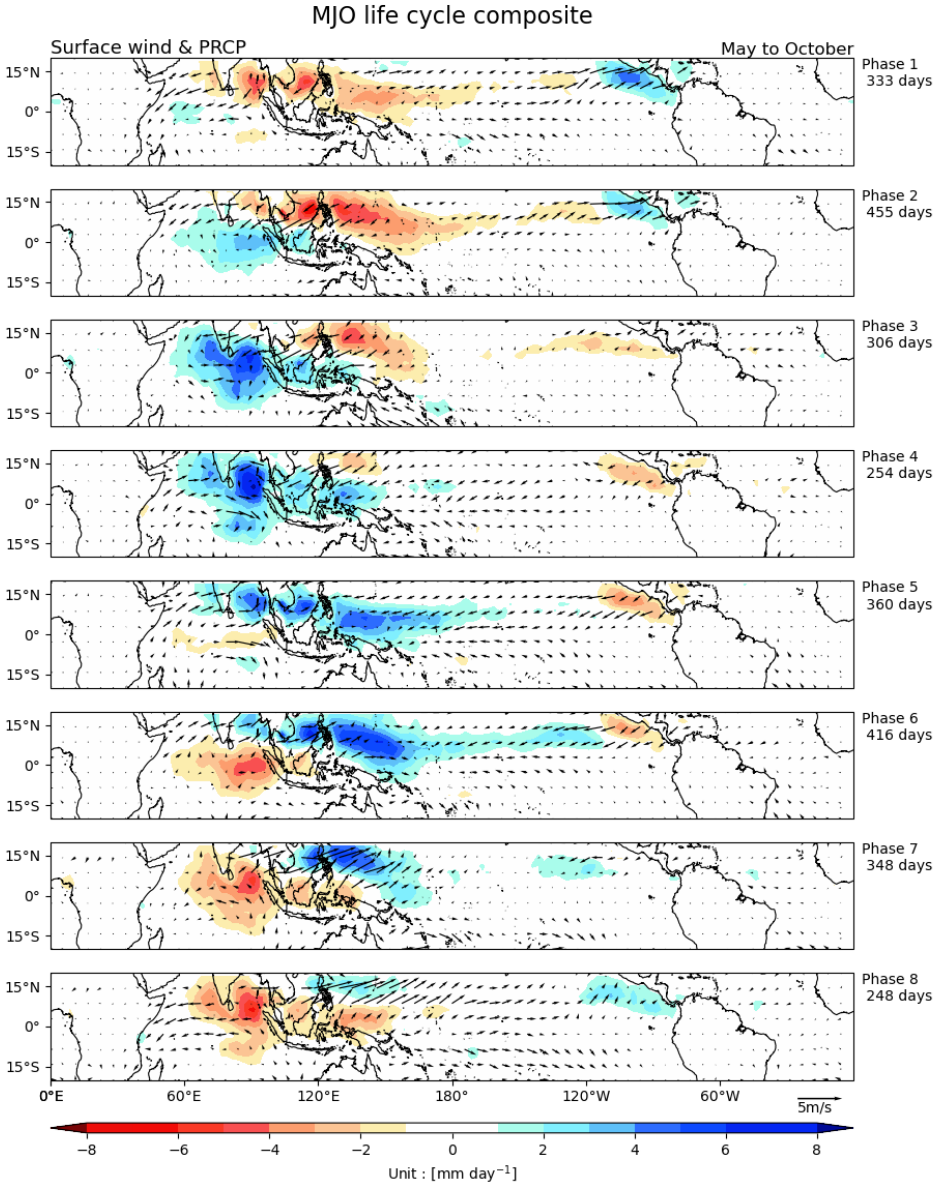

590

Figure A6 Composites of May-October intraseasonal (20-100 days) anomalies of PRCP (shades) and 10m horizonal winds (vectors) as a function of MJO phases. The number of days used to generate the composites for each phase is shown to the right of the panel.

https://doi.org/10.5194/egusphere-2026-2626
Preprint. Discussion started: 26 May 2026

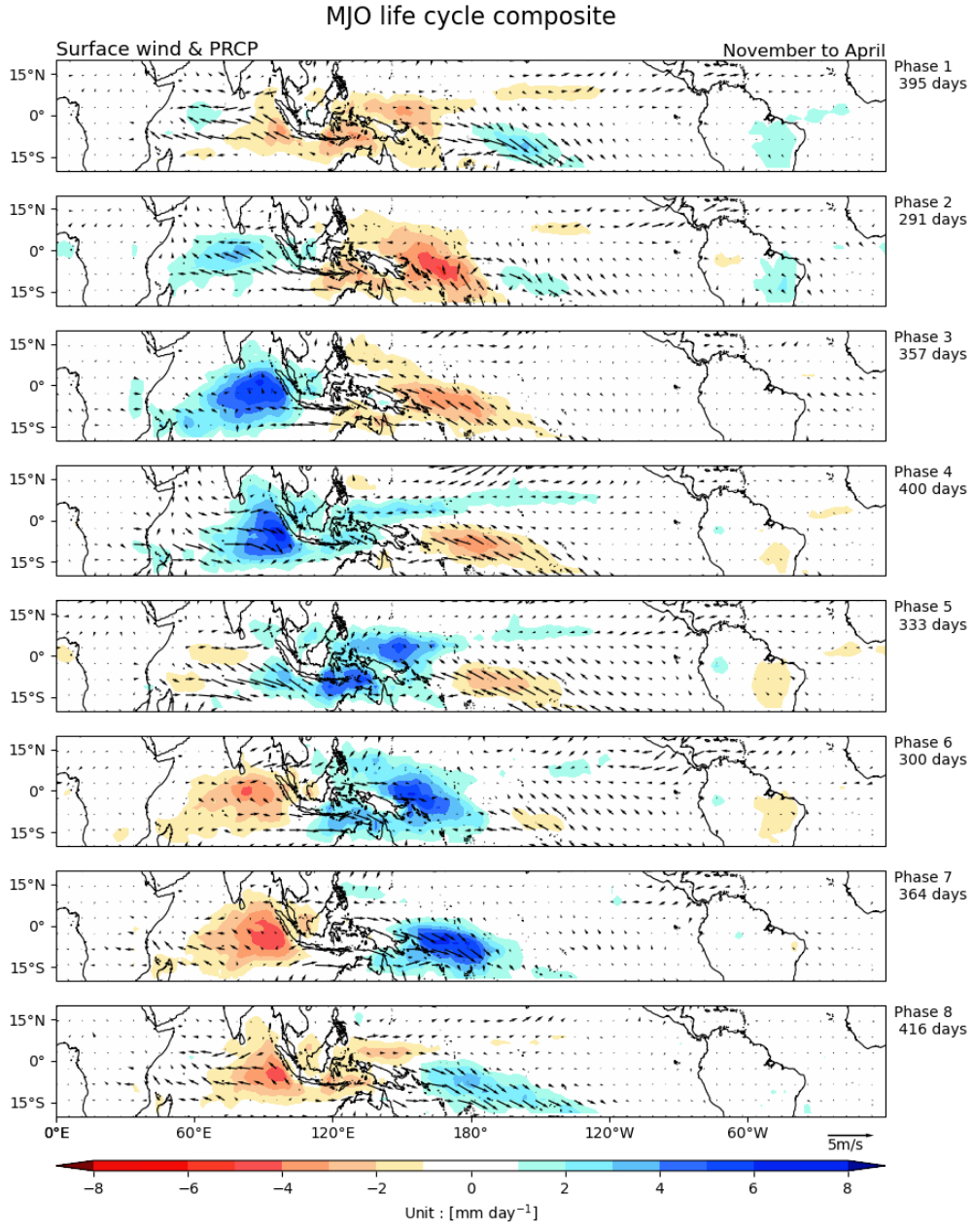

595

Figure A7 As in Fig. A6 but for November-April season.

https://doi.org/10.5194/egusphere-2026-2626
Preprint. Discussion started: 26 May 2026

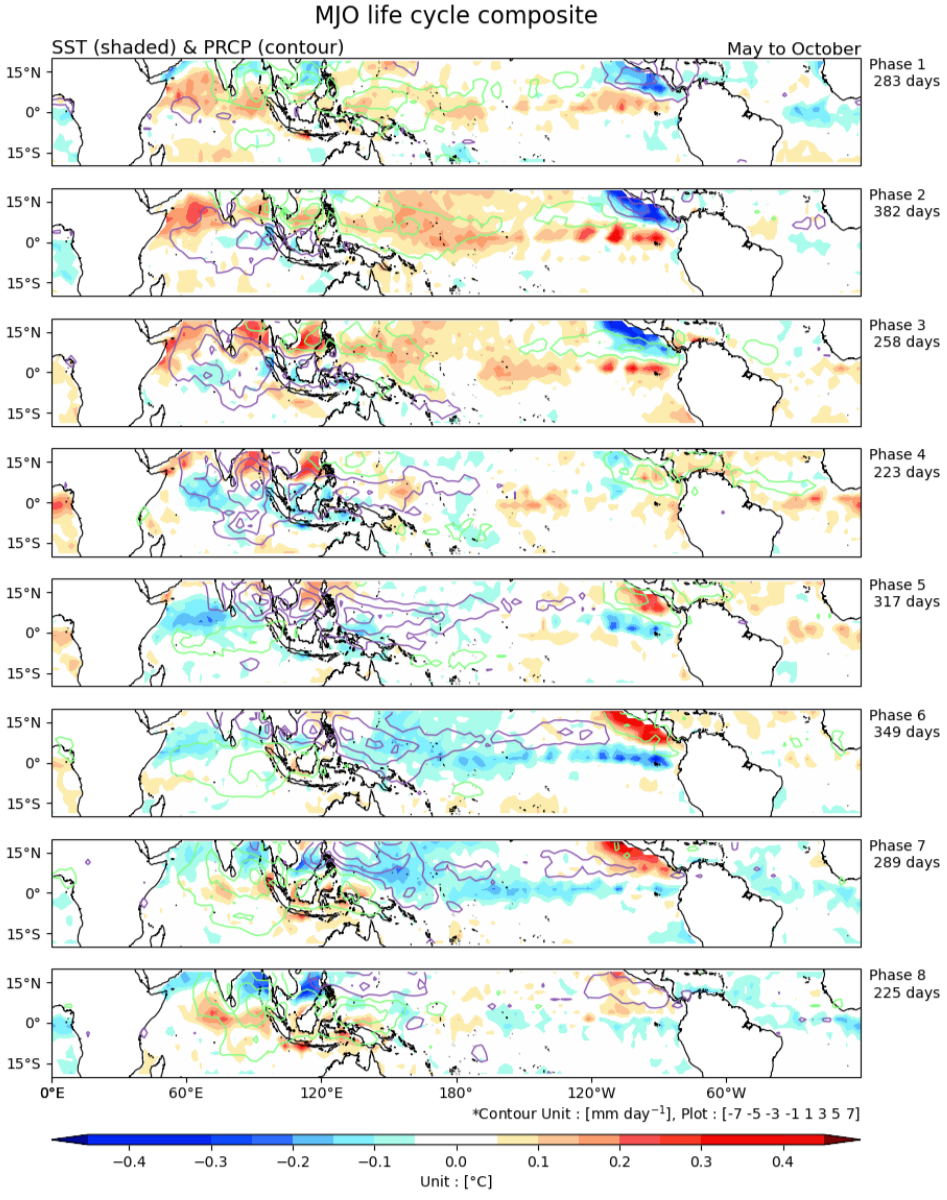

600 **Figure A8** Composites of May-October intraseasonal (20-100 days) anomalies of SST (shades) and PRCP anomalies (contours) as a function of MJO phases. The number of days used to generate the composites for each phase is shown to the right of the panel.

https://doi.org/10.5194/egusphere-2026-2626
Preprint. Discussion started: 26 May 2026

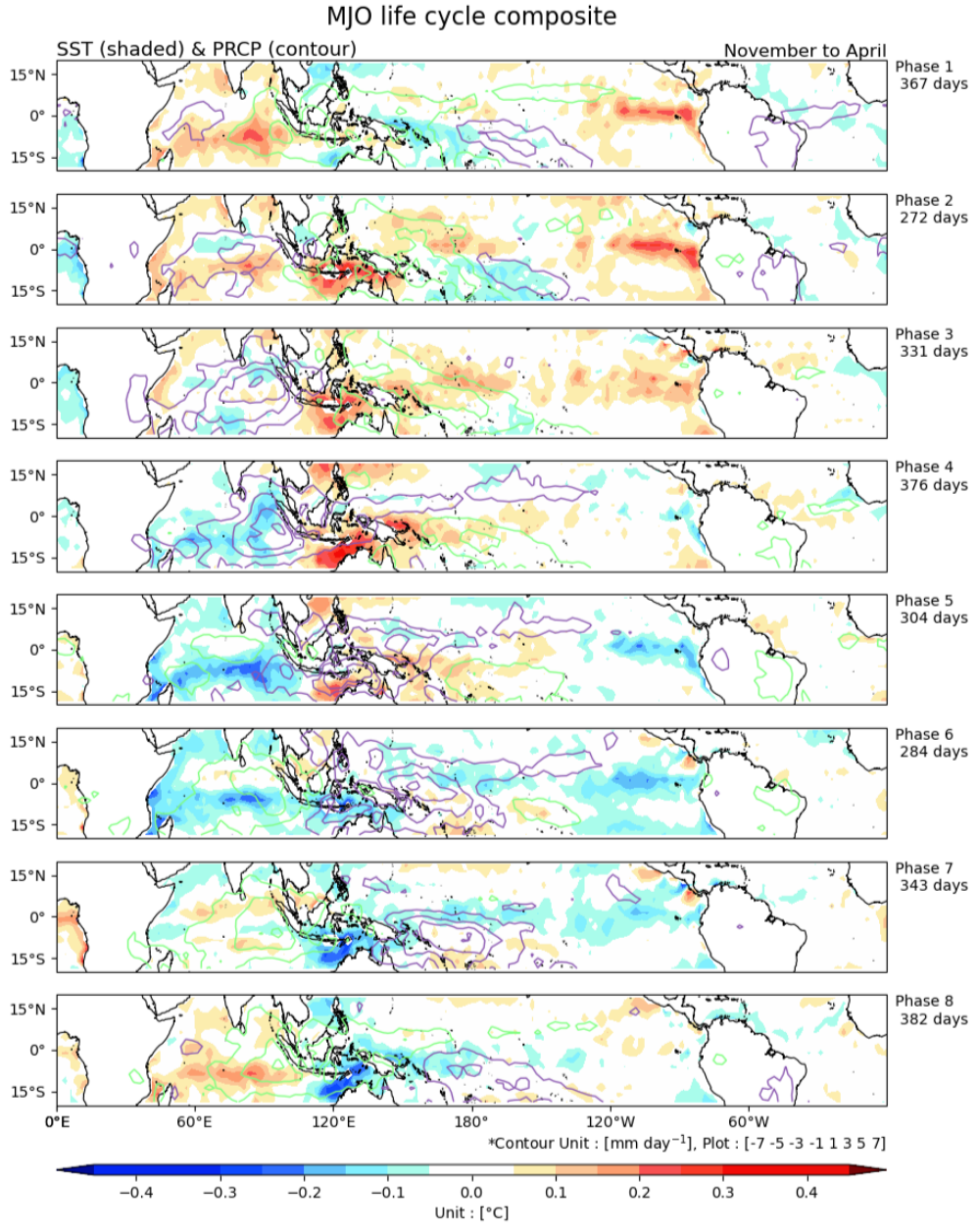

605

Figure A9 As in Fig. A8 but for November-April season.